

ShapeGaussian: HIGH-FIDELITY 4D HUMAN RECONSTRUCTION IN MONOCULAR VIDEOS VIA VISION PRIORS

Zhenxiao Liang¹, Ning Zhang², Youbao Tang², Ruei-Sung Lin²,
 Qixing Huang¹, Peng Chang², Jing Xiao²

¹The University of Texas at Austin

²PAII Inc.

ABSTRACT

We introduce *ShapeGaussian*, a high-fidelity, template-free method for 4D human reconstruction from casual monocular videos. Generic reconstruction methods lacking robust vision priors, such as 4DGS, struggle to capture high-deformation human motion without multi-view cues. While template-based approaches, primarily relying on SMPL, such as HUGS, can produce photorealistic results, they are highly susceptible to errors in human pose estimation, often leading to unrealistic artifacts. In contrast, ShapeGaussian effectively integrates template-free vision priors to achieve both high-fidelity and robust scene reconstructions. Our method follows a two-step pipeline: first, we learn a coarse, deformable geometry using pretrained models that estimate data-driven priors, providing a foundation for reconstruction. Then, we refine this geometry using a neural deformation model to capture fine-grained dynamic details. By leveraging 2D vision priors, we mitigate artifacts from erroneous pose estimation in template-based methods and employ multiple reference frames to resolve the invisibility issue of 2D keypoints in a template-free manner. Extensive experiments demonstrate that ShapeGaussian surpasses template-based methods in reconstruction accuracy, achieving superior visual quality and robustness across diverse human motions in casual monocular videos.

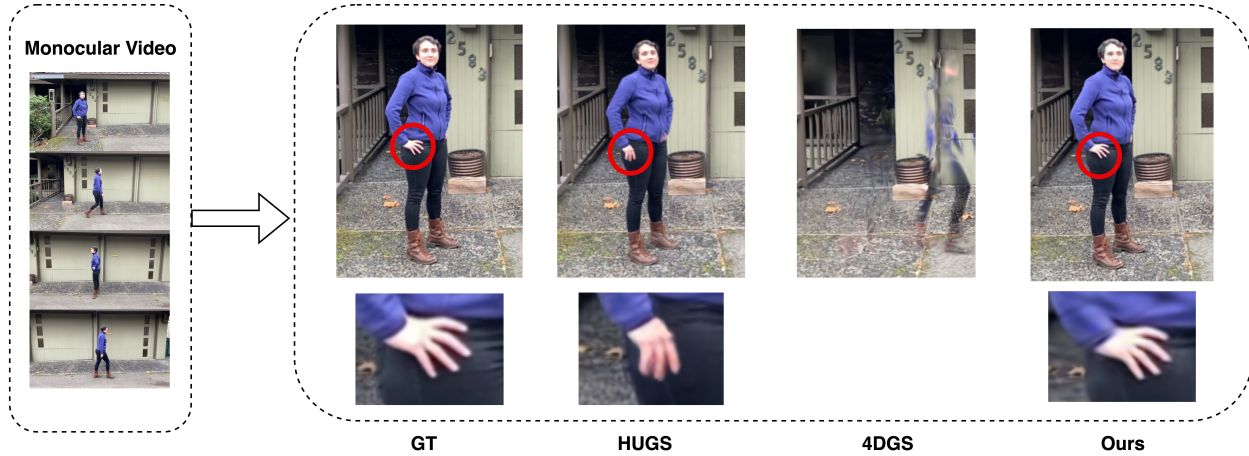


Figure 1: We propose *ShapeGaussian* to achieve high-fidelity dynamic scene reconstruction from monocular, human-centric videos in a template-free manner. Generic reconstruction methods without robust vision priors, such as 4DGS [1], struggle to capture high-deformation human motion without multi-view cues. Although template-based approaches (primarily SMPL [2]) such as HUGS [3] can produce photorealistic results, they are susceptible to errors in human pose estimation, often leading to unrealistic artifacts that compromise applicability. In contrast, our method delivers both high-fidelity and high-quality scene reconstructions by incorporating template-free vision priors effectively.

1 Introduction

Reconstruction of photo-realistic dynamic 3D scenes is an active research topic in computer vision, with broad applications ranging from video game synthesis to robotic manipulation. Recently, significant progress has been accomplished to recover this 4D representation from synchronized multi-view videos using Gaussian Splatting [4, 5, 6, 7, 8]. Yet, such specific set-up limits its applicability for daily, causal usage. In contrast, 4D reconstruction from a monocular video has more practical appeal.

A significant limitation of existing Gaussian-based reconstruction methods is their poor performance on monocular video captures featuring rapid human motion, particularly in novel view synthesis. This deficiency primarily stems from the inaccurately reconstructed geometry of the Gaussians, compounded by the unconstrained nature of the optimization problem due to the limited multi-view cues available from monocular captures. Although recent efforts have attempted to address this issue by incorporating explicit mesh-based priors into monocular video-based Gaussian avatars, these methods still struggle with reconstructing loose clothing and hair, as well as the variable and smooth appearance of the human subject over time.

State-of-the-art approaches [9, 10, 11, 3, 12, 13] for 4D human Gaussian Splatting are based on SMPL [2], a parametric 3D model of the human body. With this strong prior knowledge of 3D human shape, the result of 4D Gaussian Splatting from a monocular video is greatly improved. However, SMPL has its limitations. It doesn't fit some special local shape such as hair contour, loose clothing etc. In addition, SMPL describes statistical human shapes, so it won't fit the bodies in the video perfectly. Further, the performance of 3D human pose estimation based on SMPL deteriorates when the human subjects are strongly, partially occluded. Inaccurate pose estimation produces inaccurate 4D Gaussian splatting with statistically estimated information, which can be unsatisfactory in reconstruction tasks requiring high fidelity.

To address these challenges, we propose ShapeGaussian, a template-free method for high-fidelity, photorealistic dynamic reconstruction of human-centric scenes. Instead of relying on templates, we leverage vision foundation models [14, 15] for accurate human segmentation and detailed relative depth estimation, providing rich 2.5D information per frame. To track human shapes across frames, we adopt image correspondence models like DensePose [16] for tracking dense keypoints. By incorporating dense temporal correspondences and refining 3D surface estimates, our method achieves superior reconstruction quality. During training deformation network, we use multiple reference frames to robustly track 2D keypoints, significantly improving deformation accuracy.

Specifically, we introduce a two-step method that initially learns a coarse, deformable geometry using pretrained models that estimate data-driven priors, and then utilizes this geometry as a basis for reconstruction. In the second step, we utilize a neural deformation model to capture the dynamic deformation details, building upon the dynamic coarse point template. In short, we propose *ShapeGaussian*, and our contributions are as follows.

- We leverage 2D vision priors to address human-centric scene reconstruction from monocular videos, mitigating artifacts caused by erroneous pose estimation in explicit human template-based methods.
- We employ multiple reference frames to resolve the invisibility issue of 2D keypoints in a template-free manner.
- Extensive experiments demonstrate that ShapeGaussian outperformed template-based methods in the reconstruction task.

2 Related Work

Given our primary objective of dynamic 3D scene reconstruction involving high-deformation human motion from monocular videos, the related work is organized into two main areas. First, we examine popular representations used to model generic dynamic scene, particularly those tailored to handle complex and deforming objects. This will be discussed in Section 2.1. Second, due to absence of multi-view clues in monocular videos, it is critical to obtain a superior model initialization and strong regularization from vision models. We explore works for obtaining accurate correspondences and tracking information in Section 2.2.

2.1 Dynamic Reconstruction with 3D Gaussians

The recent rise of 3D Gaussian Splatting (3DGS) [4] highlights its capability for real-time rendering, thanks to its explicit point cloud format. Recent advancements have extended 3DGS to dynamic 3D scene modeling. Generally speaking, we can classify the representations of general dynamic scene with Gaussian Splatting into two categories.

The first approach involves using a neural network to predict deformed 3D Gaussians [1, 5, 17, 18, 19, 20]. For instance, Yang et al.[5] proposed a method that predicts Gaussian property offsets from a single reference frame using an MLP

network. Wu et al.[1] introduce a deformation field employing the efficient Hexplane representation [17]. Liu et al.[20] leverages an invertible MLP architecture, based on[21], to mitigate issues of missing Gaussians in single-frame references.

The second approach models Gaussian trajectories using a low-rank representation [22, 23, 5], which effectively captures smooth deformations as combinations of basis functions. This yields strong results for casual monocular videos with largely rigid motions, given the assumption that the deformation can be decomposed efficiently.

Our method aligns with the first approach, prioritizing flexibility to accommodate high-deformation human motion. Unlike prior methods, we incorporate multiple reference frames rather than relying solely on a single frame, enhancing performance for complex human movements. Additionally, our approach preserves an explicit canonical point cloud, which supports better geometric regularization than the virtual canonical space utilized by [20].

2.2 Correspondences and Tracking for Human Motion

Monocular 3D long-range tracking remains relatively underexplored in the literature. The most common strategy to achieve high-quality long-range 3D tracking is by lifting 2D tracking information into 3D space [22, 23, 8, 24, 25, 26]. Traditional 2D tracking approaches primarily depend on optical flow to determine point correspondences across frames [27, 28, 29, 30, 31, 32, 33, 34, 35, 36, 37, 38, 39], which has shown efficacy for short-term tracking. However, maintaining accurate tracking over extended video sequences remains a challenge due to cumulative error and the inherent limitations of optical flow in capturing long-range dependencies. Early methods for long-term 2D trajectory estimation often relied on hand-crafted priors to infer motion trajectories, allowing for limited temporal coherence.

Recently, renewed interest in long-term 2D tracking has led to promising results on challenging, in-the-wild video data. Some approaches rely on test-time optimization, where models refine noisy, short-range motion estimates into a consolidated global representation, producing stable long-term correspondences [40, 21]. Others employ data-driven techniques [41, 42, 43], leveraging synthetic data to train neural networks to predict long-term correspondences directly. While these methods achieve impressive results, they often struggle with high-deformation human motions and scenarios with rapid camera movement, as they are optimized for smoother, predictable motion. Moreover, the latest advanced preprocessing methods [44, 41, 21] for capturing 2D keypoint correspondences are typically slow, often requiring more processing time than the subsequent 3D reconstruction step.

Another common strategy involves tracking optimization techniques that rely on test-time adjustment with predefined human template, typically focusing on single human and novel pose synthesis[3, 45, 46, 47, 12, 10, 48, 49, 50, 51, 52, 3]. Although effective for isolated, consistent human, this approach is limited in dynamic scenes involving multiple, interacting humans due to its reliance on object-specific templates and assumptions of consistent appearance.

In contrast, our method leverages a pre-trained human correspondence model to extract robust 2D tracking points from UV maps, which we then lift into 3D by aligning them with estimated depth maps. Unlike prior approaches, our method operates without template priors, making it more adaptable to complex scenes with multiple fast-moving human subjects. This enables robust and efficient 3D tracking of human motion from monocular video while maintaining flexibility across diverse and dynamic settings.

3 Preliminaries

In this sections, we briefly review the representation of 3D-GS [4] in Sec. 3.1 and the formulation of priors used by our method in Sec. 3.2.

3.1 3D Gaussian Splatting

3D Gaussians [4] serve as an explicit 3D scene representation through point clouds. Each Gaussian is defined by a 5-tuple (μ, Σ, s, o, c) , where $\mu \in \mathbb{R}^3$, $\Sigma \in \mathbb{SO}(3)$ are the 3D mean and orientation and $s \in \mathbb{R}^3$ the scale, $o \in \mathbb{R}$ the opacity, and $c \in \mathbb{R}^3$ the color. The rendering process would first project 3D Gaussians onto the 2D image plane. More specifically, given the world-to-camera extrinsics \mathbf{E} and intrinsics \mathbf{K} , the projection of the 3D Gaussians can be obtained by formula

$$\begin{aligned} \mu'(\mathbf{K}, \mathbf{E}) &:= \Pi(\mathbf{K}\mathbf{E}\mu) \in \mathbb{R}^2, \\ \Sigma'(\mathbf{K}, \mathbf{E}) &:= \mathbf{J}_{\mathbf{KE}}\Sigma_0\mathbf{J}_{\mathbf{KE}}^T \in \mathbb{R}^{2 \times 2}, \end{aligned} \quad (1)$$

where Π is the perspective projection operator, and $\mathbf{J}_{\mathbf{KE}}$ is the Jacobian matrix from the affine approximation of the projective transformation determined by \mathbf{E} and \mathbf{K} at location μ . The projected 2D Gaussians can then be efficiently

rasterized into RGB image along with the depth map via volume rendering as

$$\hat{\mathbf{I}}(\mathbf{p}) := \sum_{i \in H(\mathbf{p})} T_i \alpha_i \mathbf{c}_i, \quad \hat{\mathbf{D}}(\mathbf{p}) := \sum_{i \in H(\mathbf{p})} T_i \alpha_i \mathbf{d}_i, \quad (2)$$

where $H(\mathbf{p})$ denotes the index set of Gaussians that intersect the ray shoot from pixel \mathbf{p} , and the equivalent opacity and transmittance is calculated by

$$\begin{aligned} \alpha_i &:= o_i \cdot \exp\left(-\frac{1}{2}(\mathbf{p} - \mathbf{\mu}')^T \Sigma'(\mathbf{p} - \mathbf{\mu}')\right), \\ T_i &:= \prod_{j < i} (1 - \alpha_j). \end{aligned} \quad (3)$$

3.2 Data-driven Priors

We consider three types of data-driven priors produced by off-the-shelf pretrained models, which assist our model in inferring accurate geometry from videos that lack sufficient multi-view cues. For each training image \mathbf{I} , we have the following:

Semantic Mask. Represented by a map $\mathbf{M}_{\mathbf{I}}$, where $\mathbf{M}_{\mathbf{I}}(\mathbf{p}) = 1$ if and only if the pixel \mathbf{p} is within the human silhouette.

Depth Map. Represented by a map $\mathbf{D}_{\mathbf{I}}$, where $\mathbf{D}_{\mathbf{I}}(\mathbf{p})$ indicates the distance of the point on the front-most surface from the viewpoint. In our method, two different depth maps will be obtained to cover the global and human depth maps respectively.

Human UV Maps. Denoted by $\mathbf{z}_{\mathbf{I}}(\mathbf{p}) = (i, u, v) \in \mathbb{R}^3$ for pixel \mathbf{p} , where i denotes the part id and (u, v) is the UV coordinates associated with pixel \mathbf{p} . $i = 0$ indicates the pixel is not associated with any part.

We will explain with more details in Sec. 4.2 to demonstrate how to initialize the Gaussians and deformation field based on the off-the-shelf foundation vision clues above.

4 Method

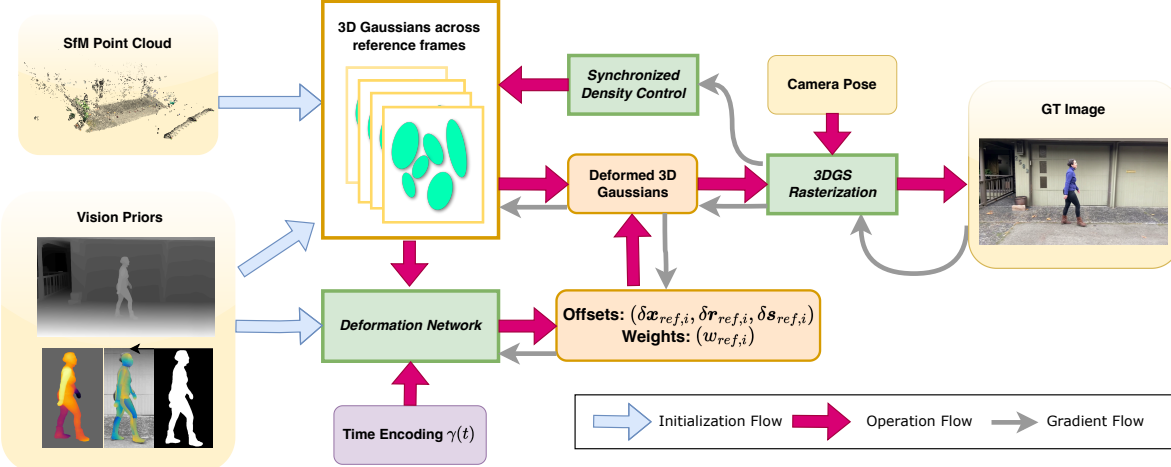


Figure 2: **Overview of our proposed method.** Initialization of the deformation network and 3D Gaussians in the reference frames is performed as described in Sec. 4.2. Following this, a joint optimization is conducted to refine both the deformation network and 3D Gaussians with synchronized density control across all frames. Yellow boxes denote all input elements, orange boxes indicate intermediate results, and green boxes represent the actions being taken.

Our method is outlined in Fig. 2. We begin by constructing a coarse dynamic Gaussian model based on vision priors derived from the input monocular video. An initial deformation field is then established to encode geometry priors. Following this, we optimize the deformation field jointly with Gaussians among reference frames, incorporating synchronized adaptive density control to ensure high-quality 4D reconstruction.

The formulation of our deformation model is detailed in Sec.4.1, followed by an explanation of the initialization process in Sec.4.2, and finally, the optimization details are discussed in Sec. 4.3.

4.1 Deformation Field

How to model the deformation across frames is a key question for dynamic scene reconstruction of a monocular sequence. We adopt a similar strategy as in [5], where a deformation field will be learned jointly with trainable 3D Gaussians.

Unlike [5], we adopt multiple frames as reference frames to overcome the issue that some Gaussians may be invisible in the single reference frame, which usually leads to terrible results for high-deformation motions, which are quite common for human-centric scene. Specifically, we select B frames of time t_1, \dots, t_B as our reference frames. We use $\bar{\mathbf{x}} \in \mathbb{R}^{B \times 3}$ to denote the collection of key point locations \mathbf{x} in the B reference frames. Given time t and location \mathbf{x} , the deformation field is defined as

$$(\mathbf{w}, \delta\bar{\mathbf{x}}, \delta\bar{\mathbf{r}}, \delta\bar{\mathbf{s}}) = \mathcal{F}_\theta(\gamma(\text{sg}(\bar{\mathbf{x}})), \gamma(t)) \quad (4)$$

where sg is the stop-gradient operation, $\gamma(r) := (\sin(2^k \pi r), \cos(2^k \pi r))_{k=0}^{L-1}$ denotes the positional encoding where L is a hyperparameter and $\mathbf{w} \in \mathbb{R}^B$ represents the weights of reference frames and is subject to $\sum_{i=1}^B w_i = 1$. $\delta\bar{\mathbf{x}}, \delta\bar{\mathbf{r}}, \delta\bar{\mathbf{s}}$ collect the offsets of location, rotation and scale, respectively, across reference frames. We then take the weighted sum of the offsets with weight vector \mathbf{w} to get

$$\mathbf{x}_t^* = \sum_{i=1}^B w_i (\bar{\mathbf{x}}_{t_i} + \delta\bar{\mathbf{x}}_{t_i}). \quad (5)$$

$\mathbf{r}_t^*, \mathbf{s}_t^*$ are calculated in a similar way. Subsequently, we put the deformed 3D Gaussians $G(\mathbf{x}_t^*, \mathbf{r}_t^*, \mathbf{s}_t^*)$ into the rendering pipeline to get the rendered image $\tilde{\mathbf{I}}_t$.

It is worth noting that some components in \mathbf{x} may be unavailable due to invisible keypoints in some frames. Further discussions on this minor issue and the details of network architecture are deferred to the appendix.

4.2 Shape-aware Initialization

Original 3D Gaussian splatting [4] relies on the sparse points from Structure-from-Motion(SfM) which are typically obtained via COLMAP [53, 54] to initialize all Gaussians locations. However, it is difficult to get a valid SfM results from a casual monocular video with significant human motions. Actually, the sparse points belonging to human body may usually be completely missing in many scenarios. Thus, we propose a shape-aware initialization scheme for our deformation model.

Alignment of depth maps. When using estimated depth maps from off-the-shelf foundational models, two main challenges arise: (1) depth estimations are typically normalized, lacking consistency with world coordinates, and (2) general monocular depth estimations often perform poorly on human bodies due to limited training data, while human-specific models fail to capture comprehensive depth cues for the broader dynamic scene. To overcome these issues, we adopt a two-step approach to generate a high-quality aligned depth map, which provides a strong basis for initializing the deformation field.

The input data to generate the aligned depth map includes 3D sparse points \mathbf{q}_i , an estimated complete depth map [15] \mathbf{D}_{com} , a human-specific depth map [14] \mathbf{D}_{hum} , and the corresponding human mask \mathbf{M} . First, we derive a sparse depth map \mathbf{D}_{sparse} from \mathbf{q}_i . We align \mathbf{D}_{com} to \mathbf{D}_{sparse} by minimizing the following alignment loss:

$$\mathcal{L}_{align} = \sum_{\mathbf{p}} |(s \cdot \mathbf{D}_{com}(\mathbf{p}) + t) - \mathbf{D}_{sparse}(\mathbf{p})|,$$

optimizing for scale s and shift t using RANSAC [55]. This produces an aligned map $\mathbf{D}_{com}^* = s^* \cdot \mathbf{D}_{com} + t^*$. Next, we perform an affine transformation on \mathbf{D}_{hum} to align it with the quantiles of $\mathbf{M} \circ \mathbf{D}_{com}^*$. We used quantiles at 0.1, 0.5, and 0.9 for alignment, which resulted in the aligned human depth map \mathbf{D}_{hum}^* . Our final aligned depth map is represented as:

$$\mathbf{D}^* = \mathbf{M} \circ \mathbf{D}_{hum}^* + (1 - \mathbf{M}) \circ \mathbf{D}_{com}^*.$$

Initialization of sparse Gaussians. Using human UV maps \mathbf{z} , we are allowed to generate consistent 2D correspondences and frame-by-frame tracking. Specifically, we interpolate on the human UV maps to identify pixel coordinates for a list of predefined IUV keypoints. These 2D points are then lifted to 3D using the aligned depth map \mathbf{D}^* . The

initial rotation of each Gaussian is determined by aligning point clouds across frames using the orthogonal Procrustes method, while all initial scales are set to a constant.

As for quasi-static background points, initialization is based on SfM points. Although the background may exhibit minor motion, the deformation field, without special initialization, can accommodate these dynamics well enough.

Initialization of deformation field. Due to significant human motion and limited multi-view constraints, we initialize the deformation field using high-accuracy sparse 3D correspondences. We lift the aligned depth map from the previous step to 3D using known camera poses, then enforce alignment with the 3D points by minimizing the following deformation loss:

$$\begin{aligned} \mathcal{L}_{deform} := & \sum_{i=1}^B \sum_{t=1}^T \sum_{\mathbf{x} \in \mathcal{G}} \mathcal{M}_{t_1, t_2}(\mathbf{x}) \left(\lambda_1 \|\mathbf{x}_{t_i}^* - \bar{\mathbf{x}}_{t_i}\|_2^2 \right. \\ & \left. + \lambda_2 \|\mathbf{r}_{t_i}^* - \bar{\mathbf{r}}_{t_i}\|_2^2 + \lambda_3 \|\mathbf{s}_{t_i}^* - \bar{\mathbf{s}}_{t_i}\|_2^2 \right) \end{aligned} \quad (6)$$

where \mathcal{G} collects all available Gaussians and $(\mathbf{x}_{t_i}^*, \mathbf{r}_{t_i}^*, \mathbf{s}_{t_i}^*)$ are determined by our deformation field (5). The mask function $\mathcal{M}_{t_1, t_2}(\mathbf{x})$ is 1 if Gaussian \mathbf{x} is visible in both t_1 and t_2 , otherwise 0. Optimization is performed on the parameters of the deformation field θ .

After this step, we discard sparse Gaussians outside the reference frames and proceed to jointly optimize Gaussians within the reference frames and the deformation field.

4.3 Optimization

The primary objective is to optimize the deformation network by minimizing the discrepancy between the rendered images and the ground-truth images from the training dataset. This involves refining the alignment between the predicted scene geometry and the actual observations, ensuring more accurate and visually consistent reconstructions.

Multi-frame density control. Adaptive density control plays an important role in original 3DGS implementation [4] to adaptively assign more Gaussians in detail-rich or high-frequency areas while prune redundant Gaussians in the plain areas. For deformation model with a single reference frame, the density control is straightforward. However, for our deformation model with multiple reference frames, we need to carefully apply the density control consistently to Gaussians over all frames. Specifically, whenever we decide to clone or split one Gaussian, we replicate this operation across all frames with recalibrated orientations.

Loss. The loss term \mathcal{L} is defined as the weighted sum of four components: L1 color loss \mathcal{L}_{color} and D-SSIM loss \mathcal{L}_{D-SSIM} comparing the rendered image $\tilde{\mathbf{I}}_t$ with the ground-truth image \mathbf{I}_t , depth loss \mathcal{L}_{depth} comparing the rendered depth map $\tilde{\mathbb{D}}$ with the aligned prior depth map \mathbb{D}^* , and the rigidity loss \mathcal{L}_{rigid} is defined similar to [22].

The final loss function is formulated as:

$$\mathcal{L} = \mathcal{L}_{color} + \mathcal{L}_{D-SSIM} + \mathcal{L}_{depth} + \mathcal{L}_{rigid}. \quad (7)$$

Training strategy. To avoid our geometry priors introduced in the initialization phase getting destructed too early due to the strong supervision from the loss, we adopt a warm-up strategy. In the initial epochs, an additional regularity loss term similar to Eq. 6 is applied to “freeze” the Gaussian locations:

$$\mathcal{L}_{freeze} = \zeta_{epoch} \cdot \sum_{t=1}^T \sum_{\mathbf{x} \in \mathcal{G}} \|\bar{\mathbf{x}}_t - \text{SRC}(\mathbf{x}_t^*)\|_2^2 \quad (8)$$

where $\zeta_{epoch} = 1 - \frac{\min(\text{epoch}, N_{freeze})}{N_{freeze}}$ decreases as the epoch count grows. Here, SRC returns the source Gaussian corresponding to \mathbf{x}_t that may have been splitted or cloned due to the density control strategy. After the first few epochs, \mathcal{L}_{freeze} gradually decreases.

5 Experiments

In this section, we assess our approach using real monocular datasets and conduct ablation studies to showcase its capability in reconstructing photo-realistic dynamic scenes featuring dramatic character action.

Datasets. First, we assess our method on the widely utilized ZJU dataset [57] under a monocular setting and demonstrate that it achieves state-of-the-art performance on objects suited to our model. Subsequently, we conducted quantitative,

		Seattle			Citron			Parking		
		PSNR \uparrow	SSIM \uparrow	LPIPS* \downarrow	PSNR \uparrow	SSIM \uparrow	LPIPS* \downarrow	PSNR \uparrow	SSIM \uparrow	LPIPS* \downarrow
4DGS	21.03	0.75	161.1	20.34	0.88	214.5	22.96	0.84	234.1	
	20.39	0.88	169.4	19.87	0.87	241.6	23.11	0.87	251.2	
	25.94	0.85	130	25.54	0.86	150	26.86	0.85	220	
	19.06	0.78	185.7	21.78	0.87	221.4	18.72	0.79	331.4	
Ours	27.68	0.90	106.4	26.51	0.91	126.4	27.15	0.89	168.2	
		Bike			Jogging			Lab		
4DGS	21.39	0.81	182.3	17.19	0.75	153.2	22.34	0.90	134.5	
	20.17	0.80	172.9	18.23	0.79	191.2	21.69	0.91	129.9	
	25.46	0.84	130	23.75	0.78	220	26.00	0.92	90	
	19.47	0.77	174.8	21.19	0.79	204.6	21.84	0.88	128.7	
Ours	26.31	0.97	98.1	24.49	0.81	124.8	27.48	0.91	79	

Table 1: Comparison of ours method with previous work on test images of the NeuMan dataset [56] using PSNR, SSIM and 1000x LPIPS metrics.

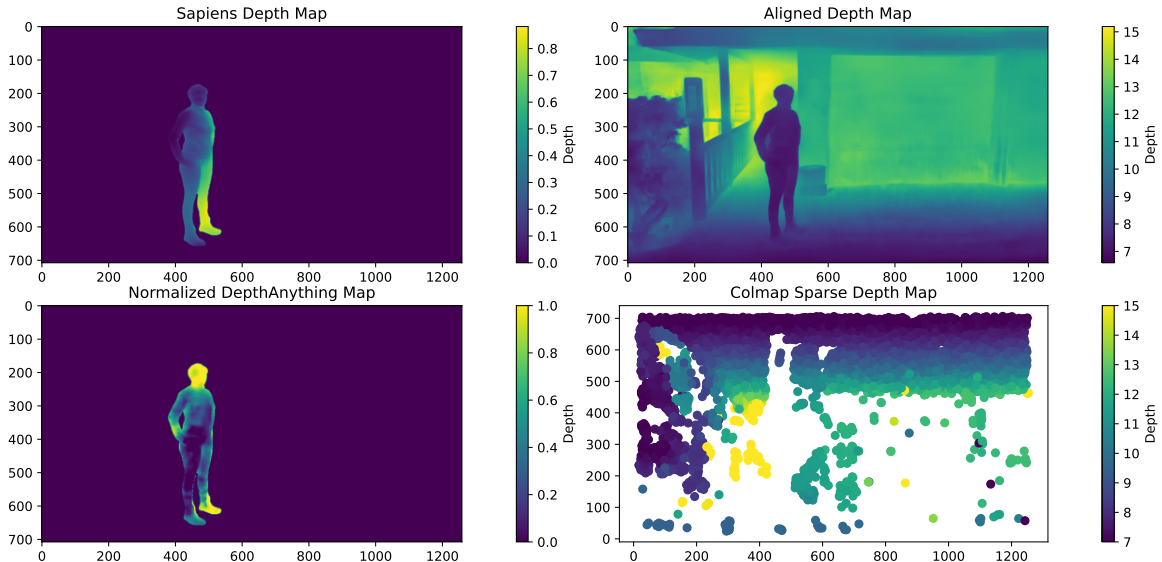


Figure 3: **Visualization of depth alignment.**

qualitative, and ablation studies on the more realistically captured NeuMan dataset [56] to show that our method effectively provides adequate regularization for this under-constrained scenario, characterized by a camera moving around a human in motion.

Comparison Methods. We evaluate our methods against two classes of approaches: neural deformation methods and avatar fitting methods. The former category includes 4D Gaussian [1] and Deformable Gaussian [5]. The latter category comprises GART [11] and HUGS [3]. Shepe-of-Motion [22]

Implementation Details. We implement our method using PyTorch [58] and conduct the differentiable Gaussian rasterization with the gsplat framework [59] which provides both rgb and depth rendering. For training, the first 5k iterations are used to optimize the deformation network, and the remaining iterations are used to optimize the 3D Gaussians in reference frames and deformation field jointly. For optimization, a single Adam optimizer [60] is used with different learning rates for the components. The whole training process including individual preparation takes approximately 40 minutes on a NVIDIA RTX 4090.

5.1 Results

Comparison on NeuMan dataset. [56] Table 1 provides a comparative analysis of our method against existing methods on the NeuMan dataset. In particular, GART is not capable of modeling the environment other than the human. Hence

	PSNR \uparrow	SSIM \uparrow	LPIPS \downarrow
w/o HDM	24.18	0.864	0.159
w/o MF	25.95	0.883	0.141
w/o DFI	22.34	0.803	0.214
Complete	26.60	0.898	0.117

Table 2: **Ablation study.** The performance is evaluated over full images using PSNR, SSIM and LPIPS metrics on NeuMan dataset. **HDM:** Human-only depth map, **MF:** Multiple reference frames, **DFI:** Deformation field initialization

we synthesize the complete novel view by combining the human rendering generated by GART and the background scene rendering provided by 4DGS in light of the human segmentation.

Our method consistently shows superior performance across all metrics and scenarios, highlighting its effectiveness in generating high-quality reconstructions from monocular recordings. In addition, the significant performance advantage of GART over 4DGS and Deformable-GS clearly indicates the critical importance of the SMPL prior.

Figure 5 presents a qualitative comparison of our method against Deformable 3DGS [5], 4DGS [61], which lacks a human shape prior, HUGS [3], which leverages a strong human template, and Shape-of-Motion [22], which employs general data-driven priors on the NeuMan dataset. For Shape-of-Motion, we follow the authors’ official instructions for custom sequences.

Generally, Deformable 3DGS and 4DGS yield significantly lower-quality renderings from novel viewpoints and, in some cases, fail to capture the human figure in the scene due to missing geometric information. Although Shape-of-Motion integrates data-driven priors such as depth maps and long-range 2D keypoints, it performs poorly because the generic 2D keypoint correspondence algorithm, such as BootsTAP [44] that was adopted in Shape-of-Motion, fails to track correct trajectories of human. As shown in Figure 4, its 2D keypoint tracking quickly diverges from the reference frame, whereas our method which derives 2D keypoints from DensePose stably tracks human motion. While HUGS [3] performs better due to its human template, it often produces inaccurate renderings of human appearance and poses due to errors in 3D pose estimation. In contrast, our method consistently delivers high-quality reconstructions by incorporating high-quality 2D visual cues, showcasing its robustness and effectiveness in managing complex human motions.

Comparison on ZJU Mocap dataset. [57] Table 3 compares the performance of our method with other state-of-the-art techniques, namely 4DGS, Deformable-GS, HUGS*, and GART, on test images from the ZJU Mocap dataset. The evaluation focuses on various scenarios identified by their dataset numbers: 377, 386, 387, 392, 393, and 394. We adopt the same camera view settings as [62] for training and testing. Our method consistently demonstrates superior performance in terms of PSNR and SSIM in all scenarios. In the context of the LPIPS metric, our method generally achieves competitive results, sometimes outperforming others.

Depth alignment visualization. Figure 3 highlights the importance of incorporating a human-specific depth map to ensure that our model begins with an initialization featuring accurate geometry. Generic depth estimation models [15, 63] often do not produce an ordinarily consistent depth for humans. Although recent methods like MoDGS [20] address this issue by introducing additional realignment steps to mitigate this issue, we empirically observe that combining a generic depth model with a human-specific depth model achieves significantly better results in human-centric scenes while maintaining simplicity.

5.2 Ablation Study

As shown in Table 2, our ablation studies evaluated the effect of removing several key components on reconstruction performance, using the real-world NeuMan data set for evaluation. The first component investigated was the role of human-centric depth estimation. For this, we tested initializing and supervising our model using only a generic depth map [15]. The second component examined the impact of multiple reference frames by comparing it to the traditional deformation model, which is based on a single canonical frame. Lastly, we tested the necessity of initializing the deformation field using a randomly sampled deformation field, as in most previous approaches. Table 2 highlights that each of these components significantly improves the performance of the model, underscoring their importance in achieving high-quality reconstructions.

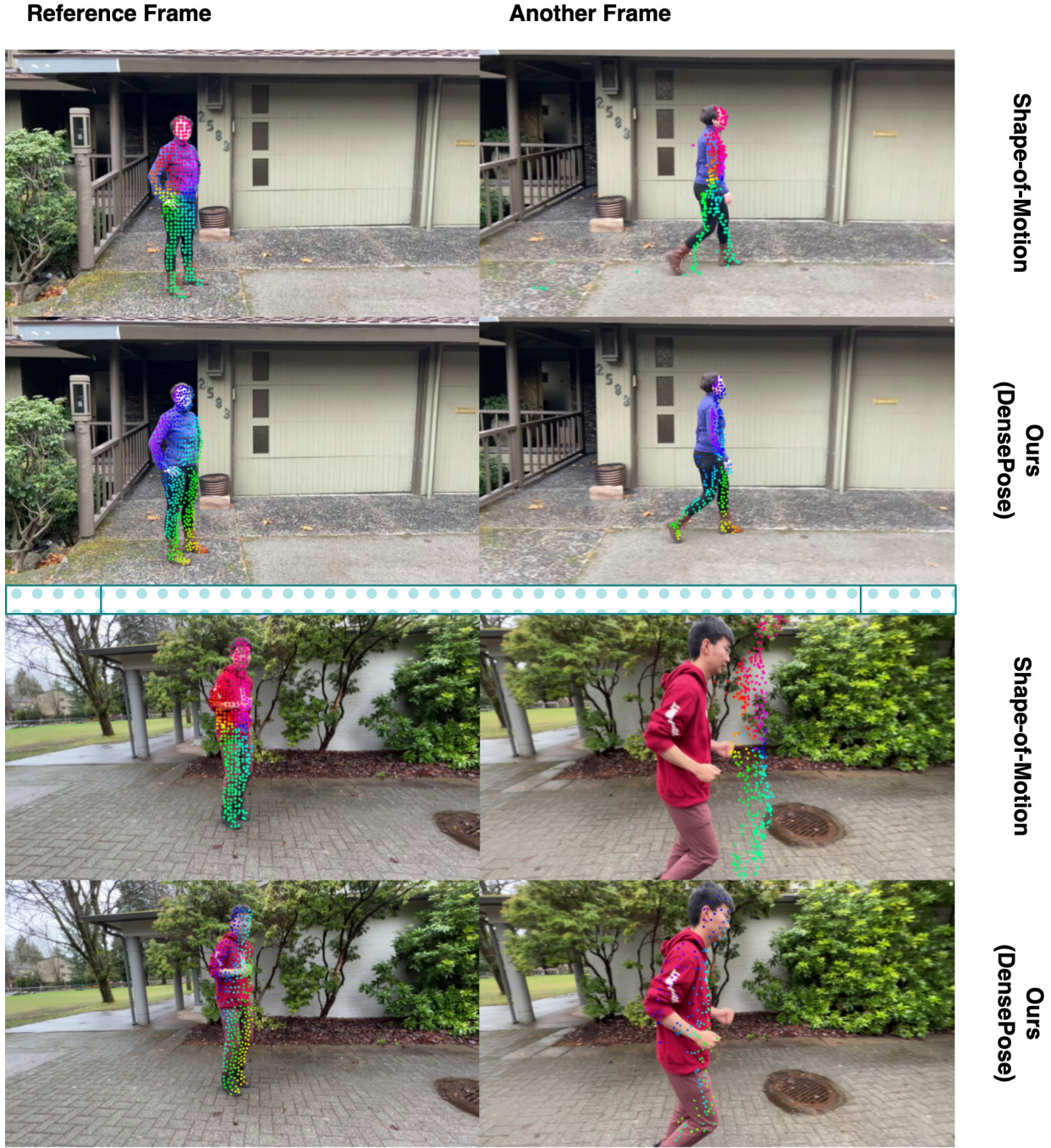


Figure 4: **Comparison of keypoint initializations.** The erroneous initialization of keypoints is the primary factor degrading the reconstruction performance of Shape-of-Motion [22] on the NeuMan dataset. Note that, for our method, we visualize only the keypoints in the other frame that remain visible in the reference frame.

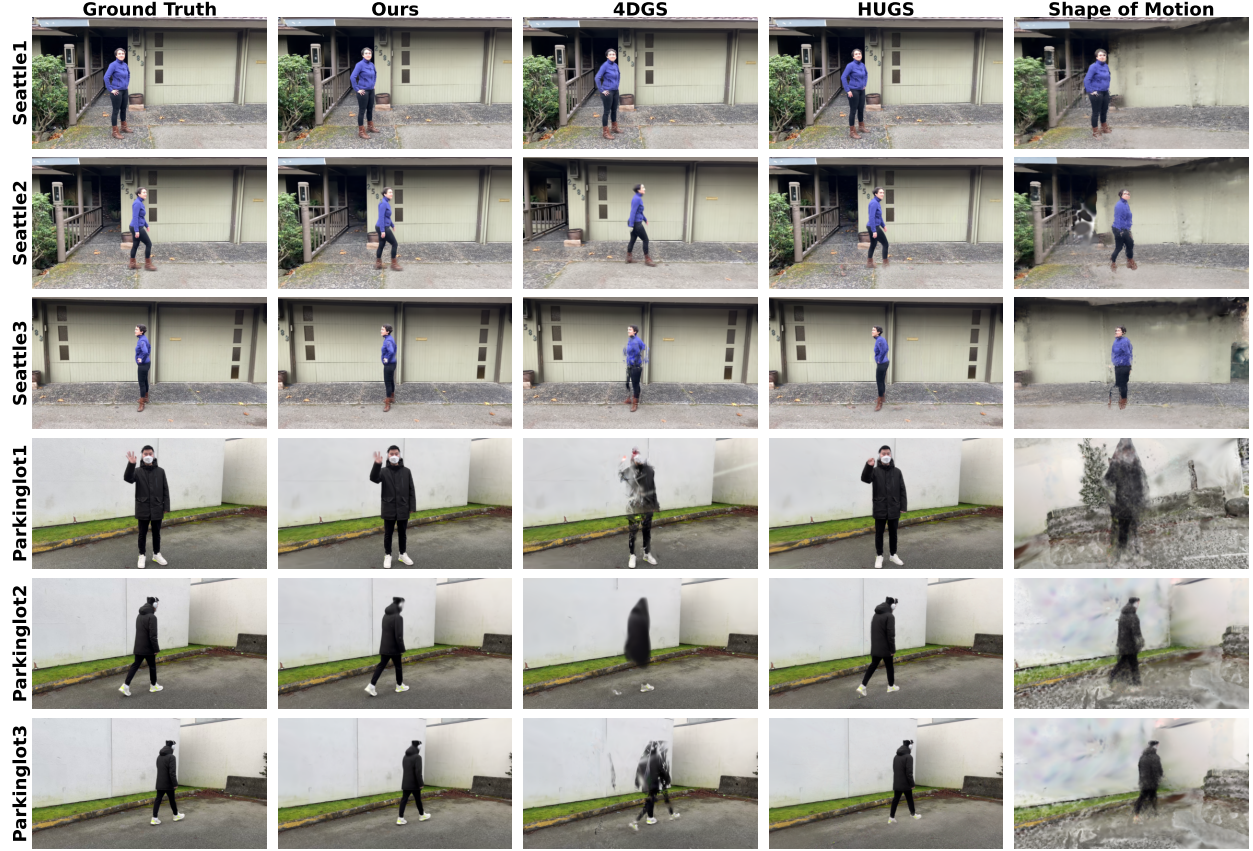


Figure 5: Qualitative comparison of baselines and our method on real dataset of casual monocular videos.

	PSNR \uparrow	SSIM \uparrow	LPIPS*
4DGS	27.18	0.84	97.2
Deformable-GS	28.49	0.86	97.7
HUGS*	30.80	0.98	20
Shape-of-Motion	26.87	0.82	102.4
GART	31.90	0.97	18.8
Ours	30.92	0.96	18.9

Table 3: Comparison of ours method with previous work on test images of the ZJU Mocap dataset [57] using PSNR, SSIM and 1000x LPIPS metrics. The evaluation results of HUGS are quoted directly from [3], and suffer from low precision for LPIPS.

5.3 Limitations

While our method can produce high-quality dynamic reconstructions from monocular videos featuring fast human motion, it faces several challenges and limitations. Firstly, our approach relies on the semantic priors provided by an external model. Moreover a set of accurate camera parameters have to be given and our reconstruction is highly sensitive to the errors of camera poses. Secondly, unlike most template-based human reconstruction work, our method cannot accommodate renderings with novel human poses. Lastly, designing a more complex model is necessary to effectively handle scenarios involving multiple people, particularly in cases with occlusions.

6 Conclusion

In conclusion, we present *ShapeGaussian*, a novel approach to capture high-fidelity dynamic scene reconstruction of human motion captured with a monocular camera. This method achieves robust and fast reconstruction while enhancing rendering quality, as validated by quantitative metrics. Unlike template-based methods, it is free from template

restriction and artifacts caused by inaccurate pose estimation, ensuring more natural and adaptable results. Technically, we introduced a novel strategy that employs multiple reference frames to effectively track invisible Gaussians in a monocular setting, overcoming key challenges in dynamic scene reconstruction.

References

- [1] Guanjun Wu, Taoran Yi, Jiemin Fang, Lingxi Xie, Xiaopeng Zhang, Wei Wei, Wenyu Liu, Qi Tian, and Xinggang Wang. 4D Gaussian Splatting for Real-Time Dynamic Scene Rendering, December 2023. arXiv:2310.08528 [cs].
- [2] Matthew Loper, Naureen Mahmood, Javier Romero, Gerard Pons-Moll, and Michael J. Black. SMPL: a skinned multi-person linear model. *ACM Transactions on Graphics*, 34(6):1–16, November 2015.
- [3] Muhammed Kocabas, Jen-Hao Rick Chang, James Gabriel, Oncel Tuzel, and Anurag Ranjan. HUGS: Human Gaussian Splatting, November 2023. arXiv:2311.17910 [cs].
- [4] Bernhard Kerbl, Georgios Kopanas, Thomas Leimkühler, and George Drettakis. 3D Gaussian Splatting for Real-Time Radiance Field Rendering, August 2023. arXiv:2308.04079 [cs].
- [5] Ziyi Yang, Xinyu Gao, Wen Zhou, Shaohui Jiao, Yuqing Zhang, and Xiaogang Jin. Deformable 3D Gaussians for High-Fidelity Monocular Dynamic Scene Reconstruction, November 2023. arXiv:2309.13101 [cs].
- [6] Jeongmin Bae, Seoha Kim, Youngsik Yun, Hahyun Lee, Gun Bang, and Youngjung Uh. Per-Gaussian Embedding-Based Deformation for Deformable 3D Gaussian Splatting, April 2024. arXiv:2404.03613 [cs].
- [7] Youtian Lin, Zuozhuo Dai, Siyu Zhu, and Yao Yao. Gaussian-Flow: 4D Reconstruction with Dynamic 3D Gaussian Particle, December 2023. arXiv:2312.03431 [cs].
- [8] Jonathon Luiten, Georgios Kopanas, Bastian Leibe, and Deva Ramanan. Dynamic 3D Gaussians: Tracking by Persistent Dynamic View Synthesis, August 2023. arXiv:2308.09713 [cs].
- [9] Yangyi Huang, Hongwei Yi, Weiyang Liu, Haofan Wang, Boxi Wu, Wenxiao Wang, Binbin Lin, Debing Zhang, and Deng Cai. One-shot Implicit Animatable Avatars with Model-based Priors, September 2023. arXiv:2212.02469 [cs].
- [10] David Svitov, Pietro Morerio, Lourdes Agapito, and Alessio Del Bue. HAHA: Highly Articulated Gaussian Human Avatars with Textured Mesh Prior, April 2024. arXiv:2404.01053 [cs].
- [11] Jiahui Lei, Yufu Wang, Georgios Pavlakos, Lingjie Liu, and Kostas Daniilidis. GART: Gaussian Articulated Template Models, November 2023. arXiv:2311.16099 [cs].
- [12] HyunJun Jung, Nikolas Brasch, Jifei Song, Eduardo Perez-Pellitero, Yiren Zhou, Zhihao Li, Nassir Navab, and Benjamin Busam. Deformable 3D Gaussian Splatting for Animatable Human Avatars, December 2023. arXiv:2312.15059 [cs].
- [13] Mengtian Li, Shengxiang Yao, Zhifeng Xie, and Keyu Chen. GaussianBody: Clothed Human Reconstruction via 3d Gaussian Splatting, January 2024. arXiv:2401.09720 [cs].
- [14] Rawal Khirodkar, Timur Bagautdinov, Julieta Martinez, Su Zhaoen, Austin James, Peter Selednik, Stuart Anderson, and Shunsuke Saito. Sapiens: Foundation for Human Vision Models, 2024. _eprint: 2408.12569.
- [15] Lihe Yang, Bingyi Kang, Zilong Huang, Zhen Zhao, Xiaogang Xu, Jiashi Feng, and Hengshuang Zhao. Depth Anything V2, October 2024. arXiv:2406.09414.
- [16] Rıza Alp Güler, Natalia Neverova, and Iasonas Kokkinos. DensePose: Dense Human Pose Estimation In The Wild, February 2018. arXiv:1802.00434.
- [17] Ang Cao and Justin Johnson. HexPlane: A Fast Representation for Dynamic Scenes, March 2023. arXiv:2301.09632 [cs].
- [18] Zhan Li, Zhang Chen, Zhong Li, and Yi Xu. Spacetime Gaussian Feature Splatting for Real-Time Dynamic View Synthesis, December 2023. arXiv:2312.16812 [cs].
- [19] Liao Wang, Jiakai Zhang, Xinhang Liu, Fuqiang Zhao, Yanshun Zhang, Yingliang Zhang, Minye Wu, Lan Xu, and Jingyi Yu. Fourier PlenOctrees for Dynamic Radiance Field Rendering in Real-time, February 2022. arXiv:2202.08614 [cs].
- [20] Qingming Liu, Yuan Liu, Jiepeng Wang, Xianqiang Lyv, Peng Wang, Wenping Wang, and Junhui Hou. Modgs: Dynamic gaussian splatting from casually-captured monocular videos, 2024.
- [21] Qianqian Wang, Yen-Yu Chang, Ruojin Cai, Zhengqi Li, Bharath Hariharan, Aleksander Holynski, and Noah Snavely. Tracking Everything Everywhere All at Once, September 2023. arXiv:2306.05422.

- [22] Qianqian Wang, Vickie Ye, Hang Gao, Jake Austin, Zhengqi Li, and Angjoo Kanazawa. Shape of Motion: 4D Reconstruction from a Single Video, July 2024. arXiv:2407.13764.
- [23] Jiahui Lei, Yijia Weng, Adam Harley, Leonidas Guibas, and Kostas Daniilidis. Mosca: Dynamic gaussian fusion from casual videos via 4d motion scaffolds, 2024.
- [24] Zhiyang Guo, Wengang Zhou, Li Li, Min Wang, and Houqiang Li. Motion-aware 3D Gaussian Splatting for Efficient Dynamic Scene Reconstruction, March 2024. arXiv:2403.11447 [cs].
- [25] Edgar Tretschk, Ayush Tewari, Vladislav Golyanik, Michael Zollhöfer, Christoph Lassner, and Christian Theobalt. Non-Rigid Neural Radiance Fields: Reconstruction and Novel View Synthesis of a Dynamic Scene From Monocular Video, August 2021. arXiv:2012.12247 [cs].
- [26] Wang Zhao, Shaohui Liu, Hengkai Guo, Wenping Wang, and Yong-Jin Liu. ParticleSfM: Exploiting Dense Point Trajectories for Localizing Moving Cameras in the Wild, July 2022. arXiv:2207.09137 [cs].
- [27] Philippe Weinzaepfel, Jerome Revaud, Zaid Harchaoui, and Cordelia Schmid. DeepFlow: Large Displacement Optical Flow with Deep Matching. In *2013 IEEE International Conference on Computer Vision*, pages 1385–1392, Sydney, Australia, December 2013. IEEE.
- [28] M.J. Black and P. Anandan. A framework for the robust estimation of optical flow. In *1993 (4th) International Conference on Computer Vision*, pages 231–236, May 1993.
- [29] Narayanan Sundaram, Thomas Brox, and Kurt Keutzer. Dense Point Trajectories by GPU-Accelerated Large Displacement Optical Flow. In Kostas Daniilidis, Petros Maragos, and Nikos Paragios, editors, *Computer Vision – ECCV 2010*, pages 438–451, Berlin, Heidelberg, 2010. Springer.
- [30] Thomas Brox, Andrés Bruhn, Nils Papenberg, and Joachim Weickert. High Accuracy Optical Flow Estimation Based on a Theory for Warping. In Tomás Pajdla and Jiří Matas, editors, *Computer Vision - ECCV 2004*, pages 25–36, Berlin, Heidelberg, 2004. Springer.
- [31] Philipp Fischer, Alexey Dosovitskiy, Eddy Ilg, Philip Häusser, Caner Hazırbaş, Vladimir Golkov, Patrick van der Smagt, Daniel Cremers, and Thomas Brox. FlowNet: Learning Optical Flow with Convolutional Networks, May 2015. arXiv:1504.06852.
- [32] Berthold K. P. Horn and Brian G. Schunck. Determining optical flow. *Artificial Intelligence*, 17(1):185–203, August 1981.
- [33] Bruce D Lucas and Takeo Kanade. An Iterative Image Registration Technique with an Application to Stereo Vision. In *IJCAI'81: 7th international joint conference on Artificial intelligence*, volume 2, pages 674–679, Vancouver, Canada, August 1981.
- [34] Xiaoyu Shi, Zhaoyang Huang, Weikang Bian, Dasong Li, Manyuan Zhang, Ka Chun Cheung, Simon See, Hongwei Qin, Jifeng Dai, and Hongsheng Li. VideoFlow: Exploiting Temporal Cues for Multi-frame Optical Flow Estimation, 2023.
- [35] Deqing Sun, Xiaodong Yang, Ming-Yu Liu, and Jan Kautz. PWC-Net: CNNs for Optical Flow Using Pyramid, Warping, and Cost Volume, June 2018. arXiv:1709.02371.
- [36] Zachary Teed and Jia Deng. RAFT: Recurrent All-Pairs Field Transforms for Optical Flow, August 2020. arXiv:2003.12039.
- [37] Haofei Xu, Jing Zhang, Jianfei Cai, Hamid Rezatofighi, and Dacheng Tao. GMFlow: Learning Optical Flow via Global Matching. In *2022 IEEE/CVF Conference on Computer Vision and Pattern Recognition (CVPR)*, pages 8111–8120, New Orleans, LA, USA, June 2022. IEEE.
- [38] Shihao Jiang, Yao Lu, Hongdong Li, and Richard Hartley. Learning optical flow from a few matches, 2021.
- [39] Shihao Jiang, Dylan Campbell, Yao Lu, Hongdong Li, and Richard Hartley. Learning to estimate hidden motions with global motion aggregation, 2021.
- [40] Michal Neoral, Jonáš Šerých, and Jiří Matas. MFT: Long-Term Tracking of Every Pixel, November 2023. arXiv:2305.12998.
- [41] Carl Doersch, Yi Yang, Mel Vecerik, Dilara Gokay, Ankush Gupta, Yusuf Aytar, Joao Carreira, and Andrew Zisserman. TAPIR: Tracking Any Point with per-frame Initialization and temporal Refinement, August 2023. arXiv:2306.08637.
- [42] Adam W. Harley, Zhaoyuan Fang, and Katerina Fragkiadaki. Particle Video Revisited: Tracking Through Occlusions Using Point Trajectories, July 2022. arXiv:2204.04153.
- [43] Nikita Karaev, Ignacio Rocco, Benjamin Graham, Natalia Neverova, Andrea Vedaldi, and Christian Rupprecht. CoTracker: It is Better to Track Together, October 2024. arXiv:2307.07635.

- [44] Carl Doersch, Pauline Luc, Yi Yang, Dilara Gokay, Skanda Koppula, Ankush Gupta, Joseph Heyward, Ignacio Rocco, Ross Goroshin, João Carreira, and Andrew Zisserman. Bootstrap: Bootstrapped training for tracking-any-point, 2024.
- [45] Zhe Cao, Gines Hidalgo, Tomas Simon, Shih-En Wei, and Yaser Sheikh. OpenPose: Realtime Multi-Person 2D Pose Estimation using Part Affinity Fields, May 2019. arXiv:1812.08008.
- [46] Tianjian Jiang, Xu Chen, Jie Song, and Otmar Hilliges. InstantAvatar: Learning Avatars from Monocular Video in 60 Seconds, December 2022. arXiv:2212.10550.
- [47] Tianjian Jiang, Xu Chen, Jie Song, and Otmar Hilliges. InstantAvatar: Learning Avatars from Monocular Video in 60 Seconds. *arXiv*, 2022.
- [48] Xinqi Liu, Chenming Wu, Jialun Liu, Xing Liu, Jinbo Wu, Chen Zhao, Haocheng Feng, Errui Ding, and Jingdong Wang. GVA: Reconstructing Vivid 3D Gaussian Avatars from Monocular Videos, March 2024. arXiv:2402.16607 [cs].
- [49] Zhijing Shao, Zhaolong Wang, Zhuang Li, Duotun Wang, Xiangru Lin, Yu Zhang, Mingming Fan, and Zeyu Wang. SplattingAvatar: Realistic Real-Time Human Avatars with Mesh-Embedded Gaussian Splatting, March 2024. arXiv:2403.05087 [cs].
- [50] Zhiyin Qian, Shaofei Wang, Marko Mihajlovic, Andreas Geiger, and Siyu Tang. 3DGS-Avatar: Animatable Avatars via Deformable 3D Gaussian Splatting, December 2023. arXiv:2312.09228 [cs].
- [51] Liangxiao Hu, Hongwen Zhang, Yuxiang Zhang, Boyao Zhou, Boning Liu, Shengping Zhang, and Liqiang Nie. GaussianAvatar: Towards Realistic Human Avatar Modeling from a Single Video via Animatable 3D Gaussians, December 2023. arXiv:2312.02134 [cs].
- [52] Zhe Li, Zerong Zheng, Lizhen Wang, and Yebin Liu. Animatable Gaussians: Learning Pose-dependent Gaussian Maps for High-fidelity Human Avatar Modeling, November 2023. arXiv:2311.16096 [cs].
- [53] Johannes Lutz Schönberger and Jan-Michael Frahm. Structure-from-Motion Revisited. In *Conference on Computer Vision and Pattern Recognition (CVPR)*, 2016.
- [54] Johannes Lutz Schönberger, Enliang Zheng, Marc Pollefeys, and Jan-Michael Frahm. Pixelwise View Selection for Unstructured Multi-View Stereo. In *European Conference on Computer Vision (ECCV)*, 2016.
- [55] M. Fischler and R. Bolles. Random sample consensus: A paradigm for model fitting with applications to image analysis and automated cartography. *Communications of the ACM*, 24(6):381–395, 1981.
- [56] Wei Jiang, Kwang Moo Yi, Golnoosh Samei, Oncel Tuzel, and Anurag Ranjan. NeuMan: Neural Human Radiance Field from a Single Video, September 2022. arXiv:2203.12575 [cs].
- [57] Sida Peng, Yuanqing Zhang, Yinghao Xu, Qianqian Wang, Qing Shuai, Hujun Bao, and Xiaowei Zhou. Neural Body: Implicit Neural Representations with Structured Latent Codes for Novel View Synthesis of Dynamic Humans, March 2021. arXiv:2012.15838 [cs].
- [58] Adam Paszke, Sam Gross, Francisco Massa, Adam Lerer, James Bradbury, Gregory Chanan, Trevor Killeen, Zeming Lin, Natalia Gimelshein, Luca Antiga, Alban Desmaison, Andreas Kopf, Edward Yang, Zachary DeVito, Martin Raison, Alykhan Tejani, Sasank Chilamkurthy, Benoit Steiner, Lu Fang, Junjie Bai, and Soumith Chintala. PyTorch: An Imperative Style, High-Performance Deep Learning Library. In *Advances in Neural Information Processing Systems*, volume 32. Curran Associates, Inc., 2019.
- [59] Vickie Ye, Rui long Li, Justin Kerr, Matias Turkulainen, Brent Yi, Zhuoyang Pan, Otto Seiskari, Jianbo Ye, Jeffrey Hu, Matthew Tancik, and Angjoo Kanazawa. gsplat: An open-source library for Gaussian splatting. *arXiv preprint arXiv:2409.06765*, 2024.
- [60] Diederik Kingma and Jimmy Ba. Adam: A method for stochastic optimization. In *International Conference on Learning Representations (ICLR)*, San Diego, CA, USA, 2015.
- [61] Zeyu Yang, Hongye Yang, Zijie Pan, and Li Zhang. Real-time Photorealistic Dynamic Scene Representation and Rendering with 4D Gaussian Splatting, February 2024. arXiv:2310.10642 [cs].
- [62] Sida Peng, Junting Dong, Qianqian Wang, Shangzhan Zhang, Qing Shuai, Xiaowei Zhou, and Hujun Bao. Animatable Neural Radiance Fields for Modeling Dynamic Human Bodies, October 2021. arXiv:2105.02872 [cs].
- [63] Clément Godard, Oisin Mac Aodha, and Gabriel J. Brostow. Unsupervised monocular depth estimation with left-right consistency, 2017.

The appendix provides more implementation details and additional experimental results to support the main paper.

	Bike	Citron	Jogging	Lab	Parkinglot	Seattle
SOM	25.27	24.95	24.05	25.94	25.78	26.31
Ours	26.31	26.51	24.49	27.48	27.15	27.68

Table 4: Comparison of PSNR between our method and Shape-of-Motion [22].

A Implementation Details

This section outlines the implementation specifics of the deformation model employed in our method, providing clarity on network design, training strategies, and practical considerations.

A.1 Deformation Model

The deformation model is based on a neural network that processes Gaussian features and predicts transformations across frames. Figure 6 illustrates our network architecture, which builds upon [5]. The embedding function γ enriches the input features by encoding spatial frequencies: γ is defined by

$$\gamma(p) := (\sin(2^k \pi p), \cos(2^k \pi p))_{k=0}^{L-1}, \quad (9)$$

where $L = 10$. An additional output channel predicts weights for each reference frame, enabling flexible and accurate deformation modeling.

During initialization, we align the deformation model with semantic priors provided by vision foundation models. The loss function defined by

$$\begin{aligned} \mathcal{L}_{deform} := & \sum_{i=1}^B \sum_{t=1}^T \sum_{\mathbf{x} \in \mathcal{G}} \mathcal{M}_{t_i, t}(\mathbf{x}) \left(\lambda_1 \|\mathbf{x}_{t_i}^* - \bar{\mathbf{x}}_{t_i}\|_2^2 \right. \\ & \left. + \lambda_2 \|\mathbf{r}_{t_i}^* - \bar{\mathbf{r}}_{t_i}\|_2^2 + \lambda_3 \|\mathbf{s}_{t_i}^* - \bar{\mathbf{s}}_{t_i}\|_2^2 \right), \end{aligned} \quad (10)$$

ensures consistency between the predicted and reference semantic priors.

After initialization, Gaussians deform according to:

$$\mathbf{x}_t^* := \sum_{i=1}^B w_i (\bar{\mathbf{x}}_{t_i} + \delta \bar{\mathbf{x}}_{t_i}),$$

where $\delta \bar{\mathbf{x}}_{t_i}$ and w_i are network outputs. For Gaussians that are not visible in certain frames, we initialize them as the mean of visible Gaussians and enforce corresponding w_i towards 0 during optimization using the regularization term

$$\mathcal{L}_{weight} := \sum_{i=1}^B \sum_{t=1}^T \sum_{\mathbf{x} \in \mathcal{G}} \left(1 - \mathcal{M}_{t_i, t}(\mathbf{x}) \right) \|w_i(\mathbf{x}, t)\|_2^2.$$

This regularization penalizes weights for invisible Gaussians, ensuring robustness in scenarios with partial visibility.

Selection of reference frames. In our method, reference frames are selected based on two criteria: (1) the union of adjacent reference frames should maximize the coverage of keypoints, and (2) the reference frames should be evenly distributed across the video. Given a predefined parameter B , representing the number of reference frames, we empirically optimize these criteria by minimizing the following cost function:

$$\begin{aligned} \mathcal{L}_{ref} := & \text{Var}(\{t_{j+1} - t_j \mid j = 1, \dots, B-1\})/T \\ & - \frac{\lambda_{ref}}{|\mathcal{P}|} \sum_i \left| \bigcup_{i \leq j < i+N_{neigh}} \mathcal{P}_{t_j} \right|, \end{aligned} \quad (11)$$

where Var computes the variance of time intervals between adjacent reference frames, \mathcal{P}_{t_j} denotes the set of keypoints visible in the j -th reference frame at timestamp t_j , and \mathcal{P} is the set of all keypoints. The parameter λ_{ref} controls the trade-off between the two criteria.

In our experiments, we set $B = 4$, $\lambda_{ref} = 0.2$ and $N_{neigh} = 3$. Since the number of reference frames is relatively small, an exhaustive search is computationally feasible to identify the optimal reference frames that minimize \mathcal{L}_{ref} as defined in Eq. 11.

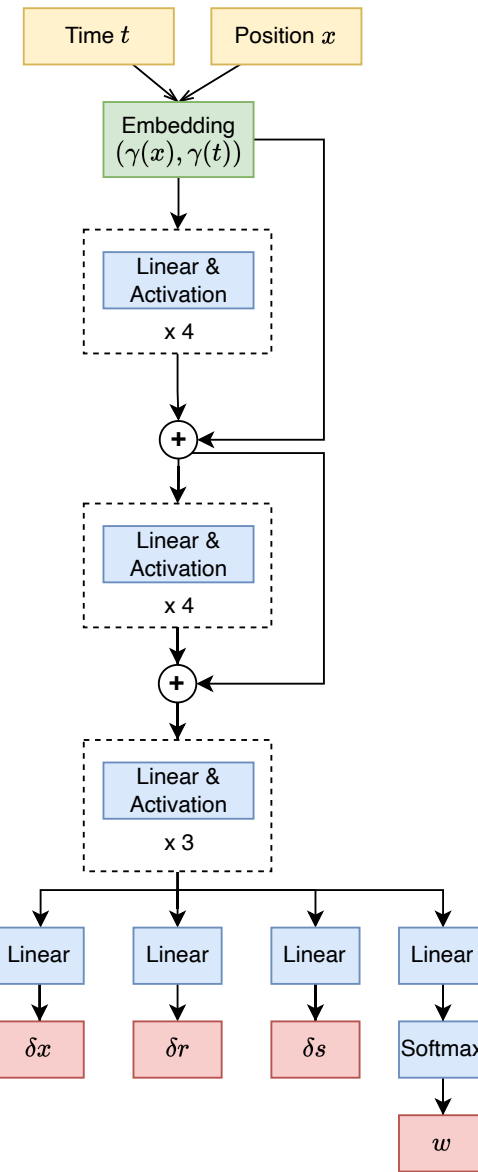


Figure 6: The network architecture for modeling deformation.

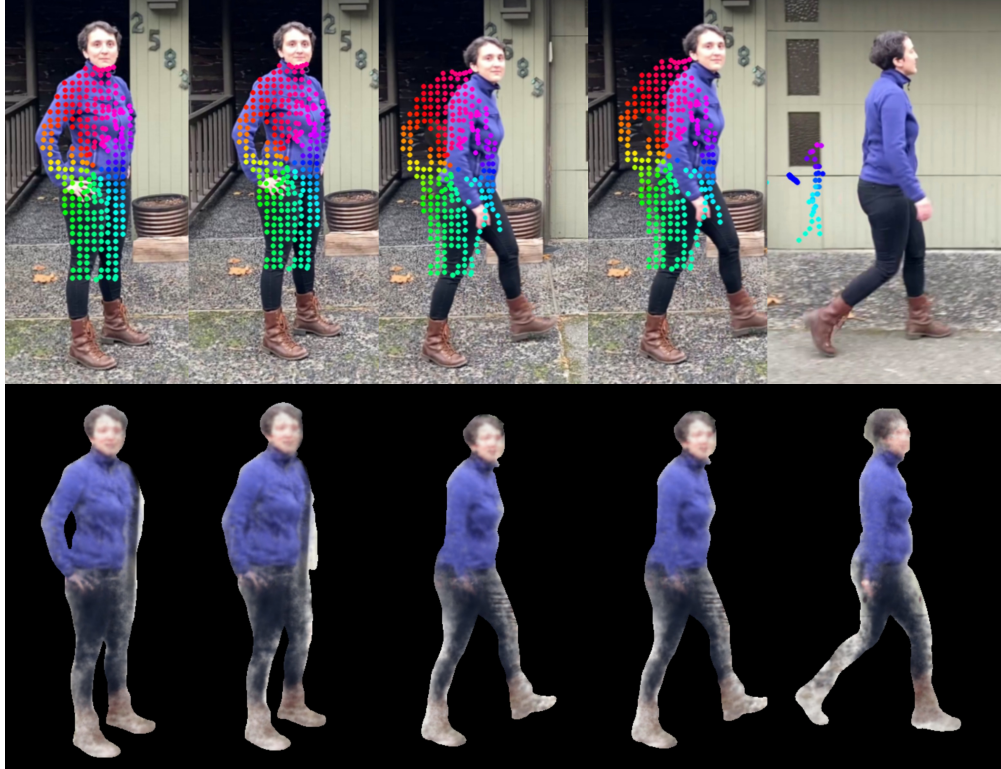


Figure 7: Shape-of-motion fails to reconstruct highly-deformable human motion due to lack of human shape priors.

A.2 Synchronized Density Control

Our method faces two primary challenges due to the use of multiple reference frames: (1) ensuring consistent density control during training to maintain the coherence of Gaussians across frames, and (2) managing the potentially large number of Gaussians, which scales with the number of reference frames. To address the second challenge, we freeze all background Gaussians and dynamically update only those associated with the human subject, significantly reducing computational overhead.

To preserve geometric consistency, when a Gaussian in one reference frame is split or cloned, we identify its k -nearest neighbors across all reference frames. These neighbors are analyzed to compute relative rotation and scaling factors, which are then uniformly applied to the corresponding Gaussians in all reference frames.

B Comparison with Generic Long-Term Tracking Methods

In this section, we detail why our method surpasses existing state-of-the-art (SOTA) methods [22, 20, 23], which rely on general long-term tracking priors. Specifically, we compare the qualitative and quantitative results of our approach with Shape-of-Motion [22], leveraging its publicly available source code. We processed casual videos following the official repository’s guidelines.

Figure 7 illustrates the limitations of Shape-of-Motion in reconstructing human-centric casual videos. The top row shows 2D keypoint tracking results, while the bottom row depicts 3D reconstructions on interpolated frames. The outputs are notably noisy and inconsistent due to the reliance on generic long-range tracking models like TAPIR [41], which lack human-specific priors. This results in frequent keypoint loss in scenarios involving fast-moving human motions and dynamic camera movements, both of which are common in casual video settings.

In contrast, our method effectively handles these challenges by incorporating human-specific priors and leveraging multiple reference frames, resulting in more robust and accurate reconstructions.